Multi-frequency aerodynamic control of a yawed bluff body optimized with a genetic algorithm

Journal of Wind Engineering & Industrial Aerodynamics 212 (2021) 104600

Contents lists available at ScienceDirect

Journal of Wind Engineering & Industrial Aerodynamics

journal homepage: www.elsevier.com/locate/jweia

Multi-frequency aerodynamic control of a yawed bluff body optimized with a genetic algorithm

Z.X. Qiao [a,*], G. Minelli [a], B.R. Noack [b,c], S. Krajnović [a], V. Chernoray [a]

[a] Department of Mechanics and Maritime Sciences (M2), Chalmers University of Technology, SE-412 96, Gothenburg, Sweden
[b] Center for Turbulence Control, Harbin Institute of Technology, Shenzhen, Xili University Town, 518058, Shenzhen, PR China
[c] Institut für Strömungsmechanik und Technische Akustik (ISTA), Technische Universität Berlin, Müller-Breslau-Straße 8, 10623 Berlin, Germany

ARTICLE INFO

Keywords:
Genetic algorithm
Yawed bluff body
Drag reduction

This experimental work aims to investigate the manipulation of a bluff body flow with a yaw angle of 10° based on a genetic algorithm optimization. Two loudspeakers are used to generate zero-net mass-flux jets through streamwise slots, which span a large portion of the rounded A-pillars of the bluff body. The actuations produce a maximum drag reduction of 17% and 2% for the leeward and windward side control, respectively. The genetic algorithm has found two typical frequencies to separately drive the actuators on the windward and leeward sides. The drag reduction is 20% under the optimal control law, 3% larger than the 17% attained from the reference single frequency control. In addition, a beneficial effect is observed when considering energy efficiency, which increases by 30% in the optimal control compared to the single frequency control. The drag spectra and velocity mapping in the wake are measured with and without control, and, based on the measurement, the underlying flow mechanism behind the control is proposed.

1. Introduction

The aerodynamic control for ground transport vehicles represents a fascinating challenge to the community of fluid dynamics due to its great potential for saving energy consumption and improving traveling safety. The control techniques for bluff bodies are usually classified into passive control and active control based on whether additional energy input is required or not. Passive control techniques such as fluidic vortex generators (e.g. Pujals et al., 2010) and flaps (e.g. Beaudoin and Aider 2008) have achieved limited success. Active control may have the potential to further improve the performance for a large range of operating conditions. Some examples include steady blowing (e.g. Aubrun et al., 2011; Zhang et al., 2018), synthetic or zero-net mass-flux jet (e.g. Minelli et al., 2016; 2019; 2020; Tokarev et al., 2019), suction and oscillatory blowing (e.g. Seifert et al., 2009), and pulsed jets with a Coanda deflection surface (e.g. Li et al., 2017). A summary of representative studies on active flow control of a bluff body in the literature is given in Table 1. Minelli et al. (2017) performed experiments to successfully suppress the side recirculation bubble using the synthetic jets, which were created through vertical slots at the front A-pillars of a bluff body. However, Minelli et al. (2019) suggested that, compared to traditionally vertical slot actuation, the streamwise slot actuation, spanning a large portion of the curvature of a rounded A-pillar, is not affected by the separation point and is thus a globally more effective actuation strategy. As a result, the present work selects the use of streamwise slots at the front A-pillars and this study is intended to shed light on the investigation of the interaction between the front and the rear separations for a yawed bluff body. Many cases of direct wake control are found in the literature, but only a limited number of works investigate the use of an upstream actuation and its effect on the wake dynamics. In addition, this method has been even less frequently tested and documented for models at yaw.

Active flow control techniques are generally conducted in an open-loop strategy, where the actuators are performed in a predetermined manner and independent of the flow state (e.g. Brunton and Noack 2015; Zhou et al., 2020). Thus, a model-based strategy is developed to improve the control performance of the actuators. A wide variety of model-based studies are available for linear models in the literature, such as local linearization of the Navier-Stokes based model (e.g. Kim and Bewley 2007; Rathnasingham and Breuer 2003), opposition or proportional-integral-derivative (PID) control (e.g. Choi et al., 1994; Hammond et al., 1998; Qiao et al., 2018), reduced-order model of the fluid dynamics (e.g. Rowley and Dawson 2017) and black-box model from input-output data sequences (e.g. Rapoport et al., 2003; Qiao et al., 2017). The challenge to model-based approach is the inherent non-linearities of turbulence, which result in a myriad of frequency crosstalk mechanisms, e.g. the large-scale instabilities of coherent structures with

* Corresponding author.
E-mail address: zengxi@chalmers.se (Z.X. Qiao).

https://doi.org/10.1016/j.jweia.2021.104600
Received 3 September 2020; Received in revised form 12 March 2021; Accepted 12 March 2021
Available online xxxx

Table 1
Summary of studies on active control for drag reduction of a bluff body reported in the literature.

Researchers	Reynolds number	Actuation technique	Yaw angle	Drag reduction
Seifert et al. (2009)	$(0.2–1) \times 10^6$	Suction and oscillatory blowing at the top and bottom trailing edges.	0	(5–20)%
Aubrun et al. (2011)	$(0.97–1.95) \times 10^6$	Steady microjet actuator array at the top trailing edge of an Ahmed body.	0	(9–14)%
Li et al. (2017)	3×10^5	Pulsed jets at all trailing edges with a Coanda deflection surface.	0	22%
Zhang et al. (2018)	1.7×10^5	Steady blowing at the edges of the rear window and vertical base of an Ahmed body.	0	29%
Li et al. (2019)	5×10^5	Pulsed jets at two trailing edges.	5°	6%
Minelli et al. (2020)	4×10^4	Synthetic jets at two front edges.	0	20%

low frequencies and energy dissipation of small vortices with high frequencies (Kasagi et al., 2009). These important frequency crosstalk mechanisms are ignored in linear control strategies, particularly in the low-dimensional control-oriented model, which further motivates the development of model-free control techniques. Model-free approaches do not rely on a dynamical model of the fluid system and only relate input parameters to outcomes with some cost function. This approach may be a useful tool for solving the issue of turbulence nonlinearity and enhancing the control performance of actuators. Some examples are the physics-based control (Zhang et al., 2004; Abbassi et al., 2017), evolutionary strategies (Koumoutsakos et al., 2001), machine learning control (MLC) (Brunton and Noack 2015; Duriez et al., 2016; Ren et al., 2020; Brunton et al., 2020) and reinforcement learning (Rabault et al., 2019).

MLC has recently been proposed to provide a promising method for manipulating a bluff-body flow by identifying the effective parameters from a rich set of possible control laws. Genetic algorithm is a powerful technique for MLC in order to optimize the control laws. Based on large-eddy simulations, Minelli et al. (2020) performed a genetic algorithm using upstream actuators at the front edges of bluff body and the effective actuation case contributes to a 20% drag reduction. However, experimental demonstration has proven to be highly challenging and few attempts have been made to manipulate the bluff-body turbulence, probably due to the difficulties in reliably measuring the aerodynamic force and implementing a practically complicated control system. Li et al. (2017) firstly found optimal control laws using linear genetic programming to actuate pulsed jets at all trailing edges of a blunt-edged Ahmed body. Approximately 33% base pressure recovery and 22% drag reduction were achieved. Following Minelli et al. (2016, 2017, 2019), Tokarev (2019) experimentally implemented a genetic algorithm to drive the blowing-suction actuators in the boundary layer at the rounded A-pillars of a bluff body model and obtained a maximum 17% drag reduction. When yaw angle is introduced, crosswind situation is reproduced. In this case, the wake behaves differently according to the separated flow around bluff body, where wake structures bend from one side to the other (Grandemange et al., 2015; Bello-Millan et al., 2016). The purpose of this paper is therefore to verify the capacity of an MLC process based on genetic algorithm to optimize the flow control law for a yawed bluff body.

This work is a continuation of the investigation of Minelli et al. (2016, 2017, 2018, 2019, 2020) and Tokarev (2019). Compared to the previous works, several differences are made to improve the aerodynamic control of bluff bodies. First, the yaw angle is changed from zero to 10°, and the flow separation is very different from the bluff body with 0-degree yaw angle. Secondly, Minelli et al. (2020) numerically implemented a multi-frequency signal to simultaneously control two upstream actuations, which was optimized with a genetic algorithm. However, the present work introduces two different sinusoidal signals to separately control the actuations on the windward and leeward front edges. As a result, the experiments based on genetic algorithm optimization are developed to reduce the aerodynamic drag for a 10-degree yawed bluff body. The experimental setup is given in Sec. 2 , and the design of genetic algorithm is presented in Sec. 3. The results and the flow physics are discussed in Secs. 4 and 5, respectively. Finally, the conclusions are drawn in Sec. 6.

2. Experimental details

2.1. The experimental set-up

Experiments were conducted in a closed-loop wind tunnel with a 3-m-long test section of 1.25 m in height and 1.8 m in width at Chalmers University of Technology. The free-stream wind speed can be varied between 0 m/s and 60 m/s. The configuration of bluff body is the same as that used in Tokarev et al. (2019), as schematically shown in Fig. 1. The bluff body, 0.36 m long, 0.4 m high and 0.4 m wide, rounded on the front edges (S_1 and S_2 A-pillars), was vertically installed in the test section. Thus, the cross-section area is A_F ($= 0.4 \times 0.4$ m^2) for bluff body and its square root value is denoted as W. The radius of A-pillar is $R = 0.02$ m as depicted in Fig. 1a. The support, connecting the bluff body to the force balance, is a symmetric NACA airfoil at zero angle of attack to minimize its aerodynamic drag. The gap between wind tunnel ground and bluff body is 0.25m to avoid the aerodynamic effect arising from the turbulent boundary layer on wind tunnel wall. The blockage ratio of the cross section of bluff body to the rectangular test section is approximately 7%. The yaw angle is set as 10° shown in Fig. 1. However, Howell et al. (2018) suggested that the contribution from the yaw angles of less than 7.5° plays a dominant role in the cycle-averaged drag coefficient in the natural environment, which is computed from the different mean incoming wind speeds and four various phases of the drive cycle, i.e., the low, medium, high, and extra high traveling phases. Furthermore, Howell et al. (2018) indicated that the drag coefficient rises with increasing yaw angle from zero to 10° and specifically, the increment on drag coefficient at 10-degree yaw angle is approximately twice that at 5°. This observation implies that at 10-degree yaw angle, the flow separation behaves much significant between two A-pillars of bluff body. As such, the effect from an asymmetric actuation may be easily captured and documented at 10-degree yaw angle, thus providing a new control method for working at low yaw angles lower than 7.5°. The support between bluff body and force balance remains at zero angle of attack with respect to the incoming wind. The force balance is also rotated counterclockwise with 10° so that the drag could be directly measured for the yawed bluff body. The coordinate system (x, y, z) is defined such that its origin o is the intersection point between the streamwise diameter of the force balance and the rear vertical base, as shown in Fig. 1 (b). The z direction is the vertical direction and its zero point is at the midpoint of the rear vertical base.

Measurements were conducted at a free-stream velocity of $U_\infty = 19$ m/s, with a flow turbulence level of 0.07%. The corresponding Reynolds number is $Re = 4.7 \times 10^5$ based on U_∞ and W. As depicted in Fig. 1a, two hot wires, mounted on the computer-controlled three-dimensional traversing mechanism, were used to characterize the flow in the wake with or without control. The sensing element of each wire was a tungsten wire of 5 μm in diameter (d) and 1.25 mm in length (l), resulting in $l/d = 250 > 200$ (e.g. Ligrani and Bradshaw 1987). Both hot wires were connected to a constant temperature circuit (Dantec 56C01 CTA) with an overheat ratio of 1.7. The signals from the wires were filtered at a cutoff frequency of 3 kHz and digitized at a sampling frequency of 10 kHz. This setting ensures that the hot wires could adequately capture the frequencies in the shear layer and in the near wake structures with a Strouhal number range of $f^* = 0.7–3.1$ or $f = 33–147$ Hz (Minelli et al.,

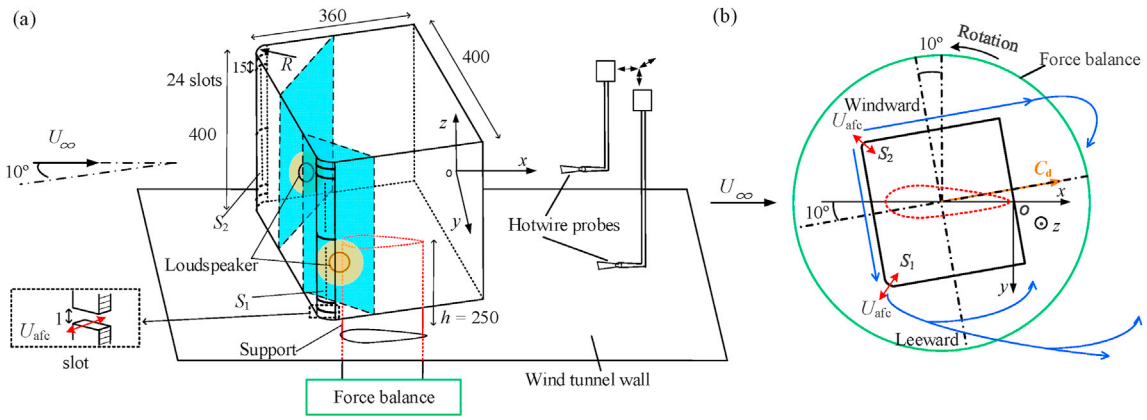

Fig. 1. (a) Schematic of experimental set-up and bluff body at a yaw angle of 10°. Dimensions of bluff body are expressed in millimeters. (b) A top view of bluff body. The red arrows indicate the actuation position and the blue lines represent the flow separation around bluff body. (For interpretation of the references to color in this figure legend, the reader is referred to the Web version of this article.)

2017). f is the frequency in Hz. In this paper, the superscript '*' denotes the normalization by W and/or the free-stream velocity U_∞, e.g. $f^* = fW/U_\infty$. The sampling duration was 20 s for each location. A total of 240 locations were sampled to recreate a 2D velocity map in the wake.

It is well known that the rounded edges of A-pillar can passively enhance the aerodynamic performance of a bluff body (Cooper 1985; Krajnović and Davidson 2003). Cooper (1985) indicated that the effect of front-edge roundness (= R/W) on aerodynamic drag coefficient is strongly influenced by the Reynolds number for bluff ground vehicles, while slightly dependent on the yaw angle when lower than 15°. In other words, at a fixed R/W, the aerodynamic drag coefficient rapidly decreases with increasing Reynolds number and then remains constant after the transcritical Reynolds number (Re_{tr}). This observation results from the effect of flow separation at the front edge with Re below Re_{tr}. Above the Re_{tr}, the flow becomes fully attached to the surface, resulting in a low drag coefficient. The transcritical Reynolds number decreases with increasing R/W, e.g., $Re_{tr} > 2.38 \times 10^6$ for $R/W = 0.05$ at 10-degree yaw angle. The present Reynolds number is below Re_{tr} and the flow separation occurs on the A-pillar of the bluff body. However, it often happens that the bluff vehicles travel at different yaw angles and Reynolds numbers. Therefore, the present study aims to optimize aerodynamic performance using the active control for low Reynolds number at the fixed R/W and yaw angle, which is still useful for practical purpose. Additionally, the flow separation may disappear on the A-pillar at the present Reynolds number if the R/W increases to reduce the Re_{tr}. However, the shape of bluff vehicles is predefined based on practical and legislative requirements, e.g., the outer dimensions of trucks (Schmidt et al., 2015). Other important aspects are the aesthetics and manufacturability. Thus, it is difficult to perform such shape optimization for passive control in the real applications.

2.2. Actuators

Two Wavecor SW182BD02-01 low-frequency loudspeaker actuators were separately installed and sealed on two A-pillars to produce blowing and suction of air flow, as shown in Fig. 1a. The r.m.s. power for each speaker is 62 W and the impedance is 8 Ohm. Each speaker was connected to separate channels of an ALTO MAC 2.4 stereo amplifier (max. power 900 W), to ensure independent controls for each actuator. The amplification of the amplifier was set as $k_a = 53$. The control signals were generated from a LabVIEW platform and then transferred to the amplifier through a 16-bit digital-to-analog (D/A) converter. The configuration and location of the A-pillars are the same as those used in Tokarev et al. (2019). Each A-pillar has 24 streamwise slots of 1 mm wide and 16 mm long and the vertical separation between the slots is 15 mm.

The actuation could be measured in terms of velocity using the hot wire at the exit of streamwise slot at a distance of 2 mm (Fig. 2a) from the opening. The actuator is driven by a sinusoidal signal $S_o = k_a A_o \sin(2\pi f)$. A_o and f are the amplitude and frequency of the sinusoidal signal generated with LabVIEW. The upper limits for A_o and f are set as 0.4 V and 250 hz ($f^* = 5.3$), respectively, to avoid possible damage on the actuators at large A_o and f. Following Minelli et al. (2017) and Li et al. (2019), the measured jet velocity is normalized by the free-stream velocity U_∞, expressed with the superscript '*' in Fig. 2. The jet flow is dominated by a weak suction and strong blowing flow, as shown in the real-time signal $U_{afc,t}$ (Fig. 2a). The hot wire is insensitive to the flow direction and measuring only velocity magnitudes so that the relatively low velocities on half actuation cycle have been inverted as negative values to indicate the weak suction. Therefore, one can clearly see a negatively low peak and a positively pronounced peak (black arrows) in every actuation cycle, which correspond to the suction and blowing phase, respectively (Minelli et al., 2017). Seifert et al. (2004, 2009) suggested that this periodic excitation is characterized by unsteady and localized energy oscillation and provides a great potential capability for altering the flow behavior, which is vastly superior to steady blowing in terms of performance. The averaged velocity profile significantly exhibits a resultant jet issuing from streamwise slots, i.e. the synthetic or zero-net mass-flux jet. The phase-averaged $\langle U_{afc,t} \rangle$ of $U_{afc,t}$ is shown in Fig. 2b where the maximum or peak jet velocity U_{afc} of $\langle U_{afc,t} \rangle$ is distinguishable and used to represent the actuation strength of actuator. Given a fixed f, U_{afc} and A_o (Fig. 2c) are correlated almost linearly, implying that the actuation strength, associated with U_{afc}, can be linearly adjusted by A_o. For a fixed A_o, the maximum value of U_{afc} takes place at $f^* = 2.1$. The maximum U_{afc} is 1.2 times that of U_∞ at $(f^*, A_o) = (2.1, 0.4\ \text{V})$, signifying that the actuation could affect the incoming flow to a great extent. Fig. 2d shows the iso-contour of U_{afc} under different control parameters (f, A_o), visualized with a contour resolution $\Delta = 0.1$. Each f is characterized by a different range of U_{afc}. In order to fully investigate the effect of the parameters (f, U_{afc}) on control performance, the range for U_{afc} needs to be limited to allow every f to possibly reach the same maximum U_{afc}. As a result, the range for f^* and U^*_{afc} has been chosen as 0.42–5.3 and 0–0.67 in Fig. 2d, respectively. Additionally, Minelli et al. (2017, 2020) proposed that these upstream actuations can further influence the wake behaviors even if the flow reattaches at the side surfaces after the rounded edges of A-pillar. As depicted in their Fig. 14 of Minelli et al. (2017), the shear layer has been attached on the side surface under the control of $f^* = 2.1$ and $f^* = 3.1$, but some significant differences are still observed between the two cases on the phase-averaged velocity streamlines in the wake. Based on proper orthogonal decomposition (POD), Minelli et al. (2020) further indicated that the upstream actuations substantially mitigate the shedding motion of the wake, thus

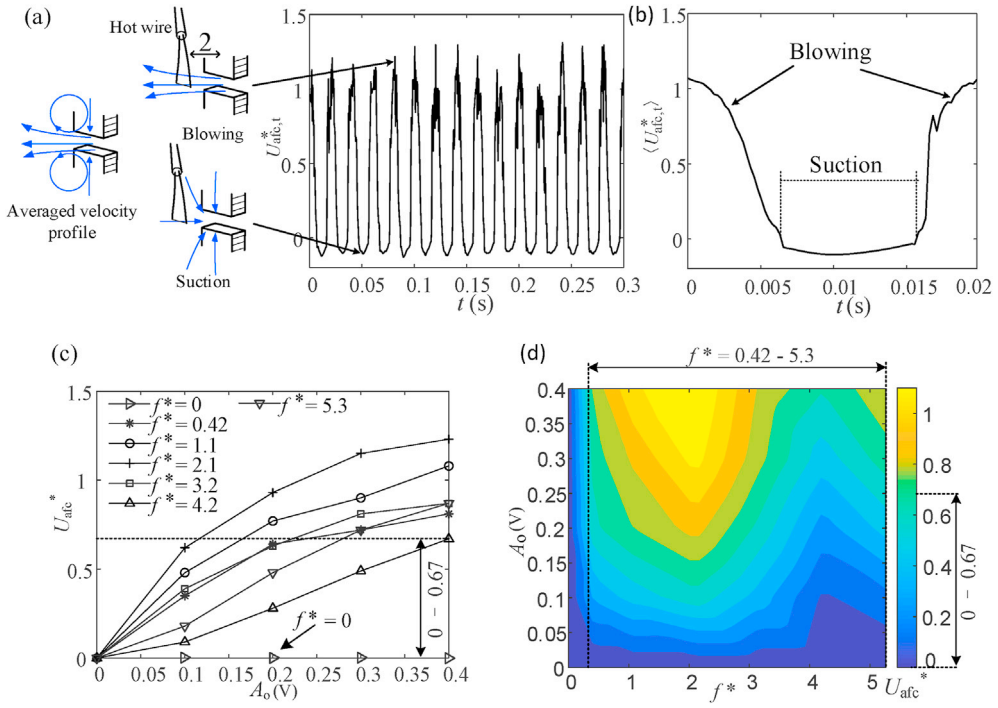

Fig. 2. (a) The real-time signal $U_{afc,t}$ under the control parameters $(f^*, A_o) = (1.1, 0.4\ \text{V})$. (b) The phase-averaged $U_{afc,t}$ of $U_{afc,t}$ under the control parameters $(f^*, A_o) = (1.1, 0.4\ \text{V})$. (c) The peak jet velocity U_{afc} of $U_{afc,t}$ under different control parameters (f^*, A_o). (d) Iso-contour of U_{afc} under different control parameters (f^*, A_o), the contour resolution $\Delta = 0.1$. $U_\infty = 0$ m/s.

improving the lateral stability and resulting in a drag reduction of 20%.

The momentum coefficient C_μ represents an indicator of the energy spent for the actuation (I_m) with respect to the energy of the unactuated flow and is defined as follows:

$$I_m = 2N_a B\rho\left(\frac{2}{T}\right)\int_0^{\frac{T}{2}} U^2_{afc,t}(t)dt \tag{1}$$

$$C_\mu = I_m \Big/ \left(\frac{1}{2}\rho W^2 U^2_\infty\right) \tag{2}$$

where N_a denotes the number of the slots on each A-pillar ($N_a = 24$), B is the area of the slot, and ρ is the fluid density. T and $U_{afc,t}$ are the actuation period and the real-time jet velocity for each A-pillar. C_μ is estimated as 2.2×10^{-3} when the actuation works with the maximum U^*_{afc}, i.e., $U^*_{afc} = 0.67$. In general, road vehicles travel at high Reynolds numbers ($Re > 5 \times 10^6$), which requires high C_μ to be effective for the actuations (Schmidt et al., 2015). Apparently, the present C_μ is too low for practical vehicles. Therefore, the present investigation merely sets an example to analyze the physical mechanism for controlling the flow around the bluff body with a yaw angle.

The present study focuses on investigating the control performance of the actuations generated on the two A-pillars for bluff body. However, it is interesting to note that the separation on the sharp edges at the front top and bottom of bluff body would also bring a significant effect on wake dynamics and aerodynamic drag, e.g., Grandemange et al. (2013), Zhang et al. (2018). Therefore, Bonnavion and Cadot (2019) introduced the chamfers at the top and bottom trailing edges to optimize the separated flow in the wake for a bluff-body model and the optimally chamfered angles lead to 6.7% of drag reduction compared to the reference squareback geometry. It may be inferred that the active actuations on the front top and bottom edges of bluff body could also optimize the wake dynamics and improve the aerodynamic performance. This study is significantly important and is expected to develop to enhance the control performance for bluff bodies in future.

2.3. Detecting and monitoring aerodynamic forces

As in Tokarev et al. (2019), the force balance is used to simultaneously measure the three-dimensional aerodynamic forces on the buff body, i.e. the drag, the side force, and the lift force. The F_d denotes the drag and C_d is the drag coefficient (Fig. 1b), which is defined as follows.

$$C_d = \overline{F}_d \Big/ \left(W^2 \overline{P}_{dyn}\right) \tag{3}$$

where the overbar denotes the time-averaged quantity and P_{dyn} is the dynamic pressure. The F_d is sampled with a frequency of 1000 Hz or $f^* = 21$, significantly larger than the main frequency range of interest $f^* = 0.7$–3.1 found in the shear layer in our previous experiments at zero yaw angle (Minelli et al., 2017). The present C_d is 1.1 under the unactuated control, which is close to that (= 1.3) for the cuboid at a yaw angle of 10° in Pirau et al. (2014). This discrepancy may be ascribed to the rounding on the front edges (S_1 and S_2 A-pillar), which could mitigate the A-pillar flow separation.

3. Genetic algorithm control design

As in Fig. 1b, it is clear that the flow separations are significantly different at the windward and leeward sides. This observation implies that separate controls on two sides may substantially improve the control performance. Based on this strategy, Li et al. (2019) experimentally used a pulsed jet strategy on either the windward or leeward trailing edge to reduce the drag of a simplified car model at a yaw angle of 5°. They found that the optimal single frequency, applied on the windward trailing edge, leads to a maximum drag reduction of 6% while the drag is increased by 4% when using the same frequency on the leeward trailing edge. A new control approach is therefore developed to overcome this drag-increased problem. In contrast to the direct-wake control approach, the present setup moves the position of the actuators upstream, thus creating an easy way to manipulate the boundary layer of the bluff body. Furthermore, the actuations on the S_1 and S_2 A-pillar are separately controlled by two

different sinusoidal signals in order to maximize the drag reduction. As such, two frequencies (f_1 and f_2) and the control law b in Fig. 3 are defined as follows.

$$\begin{cases} b_{S_1} = U_{\text{afc1}} sin\,(f_1 t) \\ b_{S_2} = U_{\text{afc2}} sin\,(f_2 t) \end{cases} \tag{4}$$

where the b_{S_1} and b_{S_2} are the control laws for S_1 and S_2 A-pillar, respectively. t is time. U_{afc1} and U_{afc2} are the peak jet velocities, and the amplitudes of the signals. f_1 and f_2 are the control frequencies for the actuators. Using 3D mapping of U_{afc}, f and A_o in Fig. 2d, the matrix T is established to transform U_{afc1} and U_{afc2} into voltages of A_1 and A_2 at different f. These voltages are used to further drive the actuators on two A-pillars. The cost function J is defined by $[(C_{\text{d}})_{on} - (C_{\text{d}})_{off}]/\ (C_{\text{d}})_{off}$, where subscripts '*on*' and '*off*' denote measurements with and without control for the yawed bluff body, respectively. J is negative and its absolute value is drag reduction. Thus, a decrease in J corresponds to an improvement on the drag reduction for a bluff body. Furthermore, the present calculation for the drag reduction just comes from the active control without optimizing the passive control parameters, e.g., above the transcritical Reynolds number for $R/W = 0.05$ at 10-degree yaw angle (Cooper 1985). However, it is reasonable that the bluff vehicles travel at different Reynolds numbers. The same calculation for the drag reduction has also been confirmed in Zhang et al. (2018) and Li et al. (2019).

The value of J is highly dependent on the chosen control law b. Thus, the optimization process searches for the best control law $b^{\star}$ to minimize J.

$$b^{\star} = \arg \min_{b} J(b) \tag{5}$$

This equation indicates a model-free optimization of multi-frequency open-loop control laws. Following Brunton and Noack (2015), Tokarev et al. (2019) and Minelli et al. (2020), the control optimization problem is solved using a genetic algorithm, which can find $b^{\star}$ in a reasonable experimental time.

In the schematic of genetic algorithm presented in Fig. 4, every generation (n) is composed of $N = 60$ individuals and every individual accounts for generating r variables ($r = 4$), i.e., two frequencies of (f_1, f_2), and two amplitudes of (U_{afc1}, U_{afc2}) in Eq. (4). Each variable is composed of m binary genes (0 and 1) and m is set as 25. Following Wahde (2008), the binary decoding is used in the evolutionary process of genetic algorithm. As introduced in Sec. 2.2, the range has been chosen as 0.42–5.3 for both f_1^* and f_2^* and 0–0.67 for both U_{afc1}^* and U_{afc2}^*.

The genetic algorithm creates $(n + 1)^{\text{th}}$ generation based on n^{th} generation. For the n^{th} generation, the control law b in the individual is defined as $b_i^{(n)}$, where i represents the number of individuals, i.e., $i = 1, 2, 3, \ldots, N$. In particular, the first population (1^{th}) is initialized by randomly generating N binary strings (individuals) $b_i^{(1)}$ of length $k = mr$. The performance of $b_i^{(n)}$ is evaluated in the experiment and denoted using the $J_i^{(n)}$, as shown in Fig. 4. Then, the $J_i^{(n)}$ is re-numbered in ascending order.

$$J_1^{(n)} \leq J_2^{(n)} \leq \ldots J_i^{(n)} \ldots \leq J_N^{(n)} \tag{6}$$

With elitism, the best i_e individuals are copied into the $(n + 1)^{\text{th}}$ generation. In the present study, the value of i_e is set as 3.

$$b_i^{(n)} = b_i^{(n+1)},\ i = 1, \ldots, i_e \tag{7}$$

The remaining N - i_e individuals of the $(n + 1)^{\text{th}}$ generation are determined by repeating three genetic operations: tournament selection, crossover and mutation. Tournament selection selects N_t individuals with equal probability for all individuals of the n^{th} generation. N_t is the tournament size and presently set as 5. The best individual is selected with the probability P_{tour} from the N_t individuals. If the individual is not selected, the next step is to repeat the procedure for the remaining $N_t - 1$ individuals, again with probability P_{tour} to select the best individual. As such, this procedure is operated until one individual is selected. In other words, this operation finds the better individuals to a certain extent without ignoring the low-performing individuals. We repeat the tournament selection to produce two individuals for conducting the crossover. The crossover carries out a wide-ranging non-local search and yields better individuals to exploit the populated local minima of J (Zhou et al., 2020). It is common to carry out crossover to breed two new individuals exchanging a part of 'genes' from both individuals with a certain probability P_c. In cases where crossover is not performed, the two selected individuals are simply copied as they are. The mutation provides

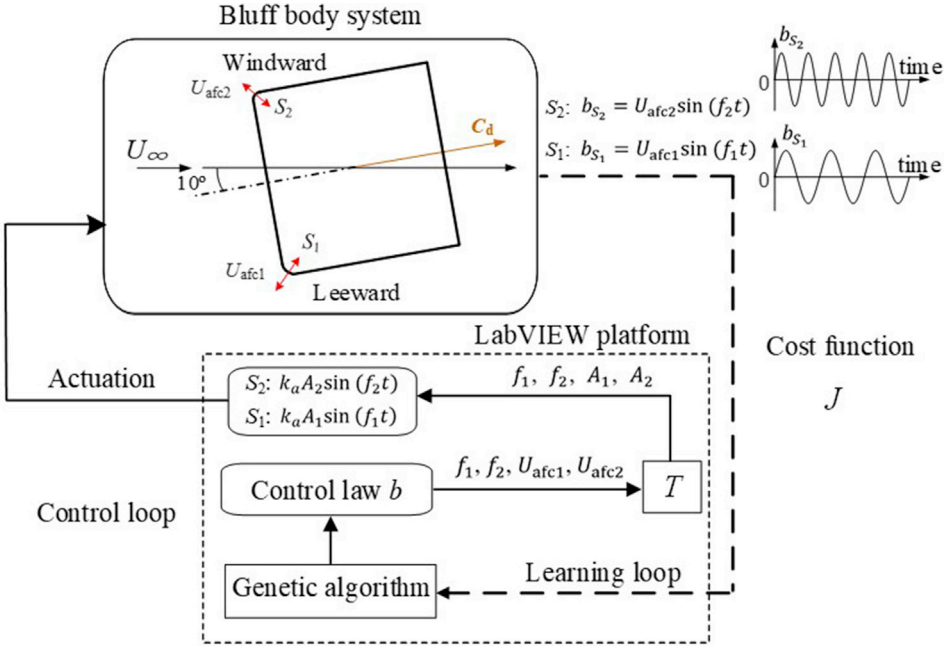

Fig. 3. Schematic diagram of genetic algorithm system. The control law is represented as $b_{S_1} = U_{\text{afc1}}\sin\ (f_1 t)$ and $b_{S_2} = U_{\text{afc2}}\sin\ (f_2 t)$ for two sides (S_1, S_2), respectively. The T is a matrix, which transforms U_{afc1} and U_{afc2} into the voltages of A_1 and A_2, to further drive the actuators on two A-pillars. The k_a is the amplification of the amplifier. J is the cost function. f_1^*, $f_2^* \in [0.42, 5.3]$, U_{afc1}^*, $U_{\text{afc2}}^* \in [0, 0.67]$.

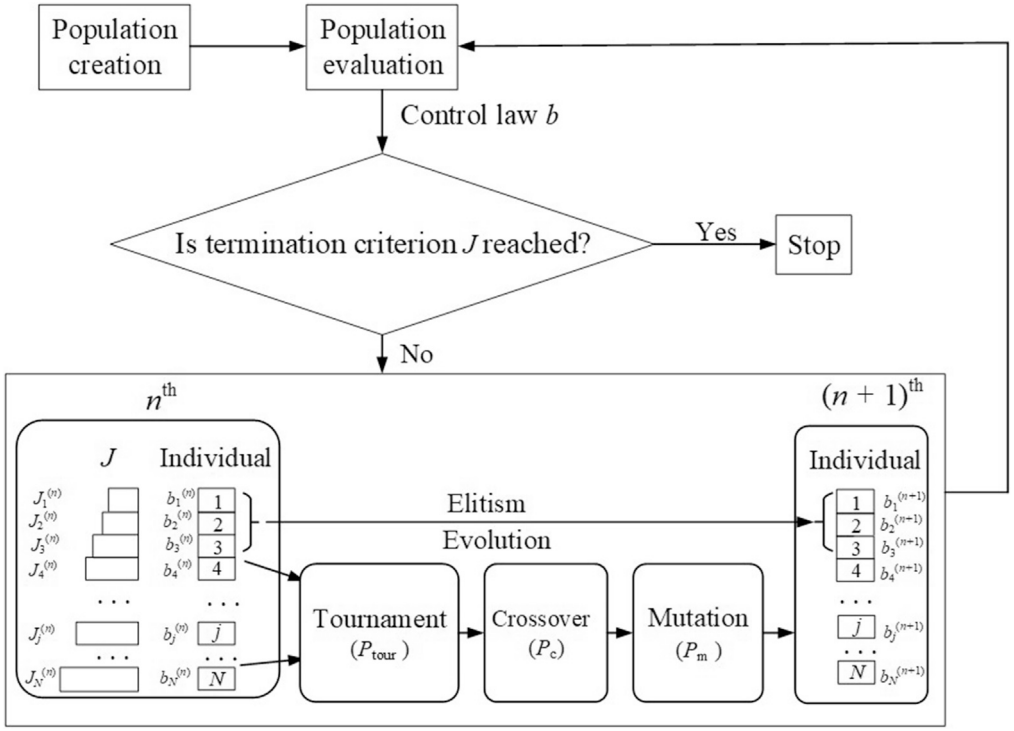

Fig. 4. Evolutionary process of genetic algorithm in machine learning control (MLC).

new individuals for evolution to explore new local minima of J. This operation has a single individual and normally consists of bit-flipping for the binary encoding schemes, i.e., a mutated 0 becomes a 1, and vice versa. The probability of mutation is defined as P_m for every individual. Since the mutation rarely has a positive effect on fitness, the value of P_m is very low and set as $1/m$. The parameters of genetic algorithm are listed in Table 2 to clarify the properties of genetic algorithm in MLC.

These iterations are performed until N individuals are created for the $(n+1)^{th}$ generation. The genetic algorithm decodes all newly generated individuals to form the four corresponding variables, i.e., f_1, f_2, U_{afc1} and U_{afc2}. Then, the LabVIEW script evaluates the performance of the actuators using the variable values obtained in each individual and assigns a corresponding $J_i^{(n+1)}$ value. As shown in Fig. 4, the evolution is repeated unless the termination criterion has been reached, where the J converges with an uncertainty of lower than 2% for the best individuals in the last 10 generations. The control law from the best individual is taken as the solution of the regression problem in Eq. (5).

The control signal is transferred between the LabVIEW platform and the actuators using a National Instrument USB-9162 multifunction I/O Device running at a sampling rate of 1000 Hz. A sampling time of 8 s is used to test every individual in each generation. As the two actuators are controlled by two different control signals, the genetic algorithm control is considered as a multi-input-single-output (MISO) system.

Table 2
Parameters of genetic algorithm in the MLC experiment.

Parameters	Value
Population size	$N = 60$
Variables	$r = 4$
Binary size per variable	$m = 25$
Binary size per individual	$k = mr = 100$
Elitism	$i_e = 3$
Tournament	$N_t = 5$, $P_{tour} = 0.75$
Crossover	$P_c = 0.8$
Mutation	$P_m = 1/m = 0.04$

Table 3
The control parameters and J values of five representative cases in Fig. 8

Case	f_1^*	f_2^*	U_{afc1}^*	U_{afc2}^*	J
A	1.47	4.44	0.01	0.54	−4.0%
B	4.01	3.75	0.50	0.66	−9.0%
C	1.37	5.10	0.32	0.61	−15.3%
D	1.33	3.87	0.50	0.63	−18.0%
E	1.42	3.84	0.67	0.63	−20.0%

4. Control performance

4.1. Single frequency control

It is crucial to first investigate the performance for control strategies using one frequency, which may facilitate the understanding of the flow physics behind the control results. Three different control strategies are investigated, i.e., single frequency control, S_1 control and S_2 control. The single frequency control means that the actuations on the S_1 and S_2 A-pillar are controlled using the same sinusoidal signal. Fig. 5a presents the iso-contours of J over the U_{afc}^* at different f^* for the single frequency control, where the minimum J is −17%, taking place in the neighborhood of $(f^*, U_{afc}^*) = (1.54, 0.67)$. With S_1 or S_2 control, the actuator is turned on for only one side while the other side is off and the slots are sealed with tape to avoid any interaction between the two A-pillars. The minimum J is −17% and −2% for the S_1 and S_2 control (Fig. 5b and c), respectively. Even though the bluff bodies are very different in their geometries, it is worth pointing out that the present upstream control obtains a significantly higher performance than the direct-wake control in Li et al. (2019), where the actuation, on the windward trailing edge, produces a maximum drag reduction of 6%. The minimum J for the S_1 control is significantly lower than that produced by the S_2 control, which suggests that the actuation, applied on the leeward side, plays a dominant role in the drag reduction and is much more effective than that on the windward side. Furthermore, the minimum region for J is slightly enlarged under the S_1 control compared to the two-side control.

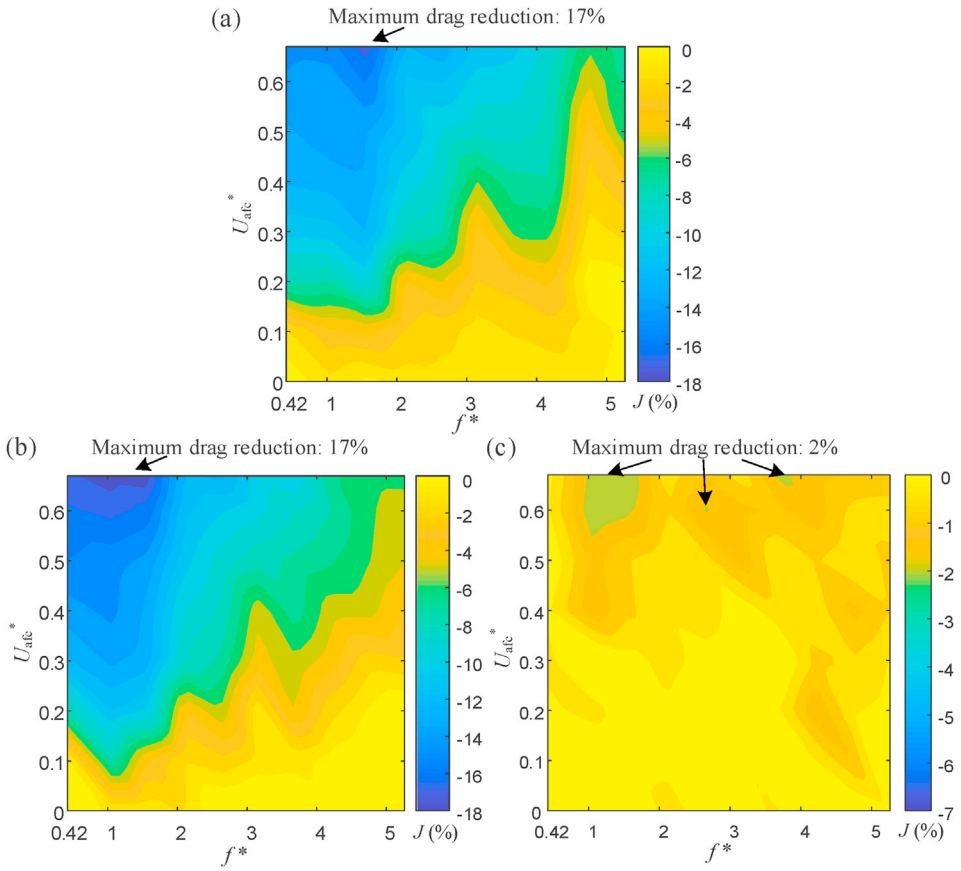

Fig. 5. Iso-contours of J over the U_{afc}* at different f* for different control strategies using one frequency. (a) Single frequency control: The actuations on the S_1 and S_2 A-pillar are controlled using the same sinusoidal signal; (b) S_1 control. S_1: on, S_2: off; (c) S_2 control. S_1: off, S_2: on. The contour resolution is $\Delta = 0.005$.

However, the S_2 control displays three minimum regions for J, which are surrounding the control parameters $(f^*, U^*_{afc}) = (1.29, 0.64)$, $(2.66, 0.60)$ and $(3.77, 0.65)$. This result implies a high possibility that the genetic algorithm may improve the control performance when the control parameters are separately optimized on two A-pillars.

4.2. Genetic algorithm control

J is used to evaluate the control performance of genetic algorithm and its evolution is presented in Fig. 6. For visual clarity, every third data between $i = 1$ and 60 is displayed, i.e., $i = 1, 4, 7, \ldots, 60$. The individuals of each generation are ordered by increasing J values following Eq. (6), where the smallest J takes place at $i = 1$, corresponding to the optimal or best control individual in every generation. The minimum value of J is approximately - 20% for $n \geq 10$. As the number of generations increases, the evolution of the J gradually converges for the first 50 individuals shown in Fig. 6. This means that the genetic algorithm generates more and more similar individuals from the former generation. Nevertheless, a number of individuals continuously explore the search space, promoting a good balance between exploitation and exploration.

A sampling time of 16 s is used to sample the optimal individuals for 8 times in each generation and the standard deviation of J has been plotted in Fig. 7. The averaged J initially decreases with increasing n and its value is between -19.6% and -20% for $n \geq 8$. The optimal control parameters are taken as $f_1^* = 1.42, f_2^* = 3.84, U^*_{afc1} = 0.67$ and $U^*_{afc2} = 0.63$, which corresponds to the best control individual for the generation $n = 21$, resulting in a - 20% of J visualized in Fig. 7. It is interesting to note that the control parameters $(f_1^*, U^*_{afc1}) = (1.42, 0.67)$ and $(f_2^*, U^*_{afc2}) = (3.84, 0.63)$ produce -17% and -1.5% for the S_1 (Fig. 5b) and S_2 control (Fig. 5c), respectively. However, the combination of the multi-frequency

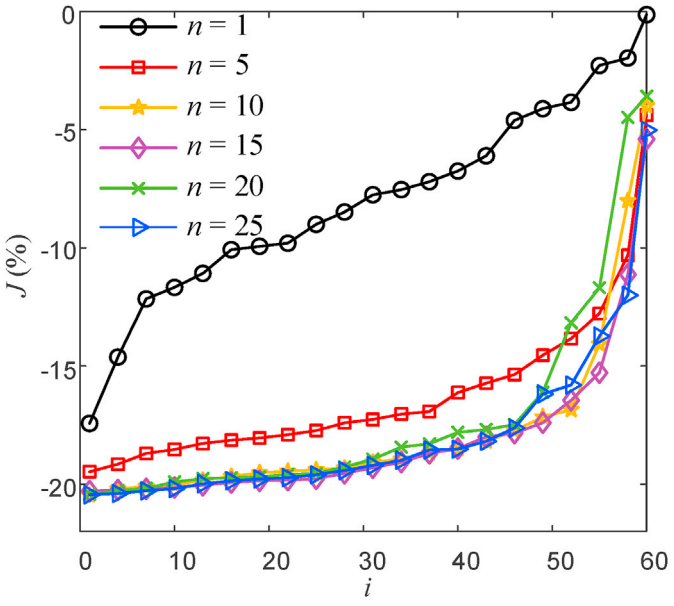

Fig. 6. Dependence of J on the individual index (i) for the different generations (n).

on two sides accounts for an improvement of 3% drag reduction, outperforming the single frequency control (17% of drag reduction in Fig. 5a).

The 'control landscapes' of all the tested individuals are represented in a proximity map using multi-dimensional scaling (MDS, Mardia et al.,

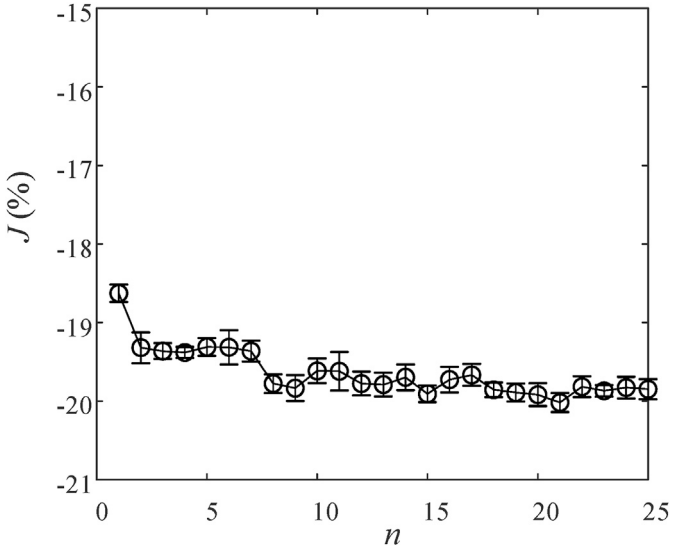

Fig. 7. J for the best individual in each generation (n). The circles indicate the averaged J values and the error bars denote its standard deviation.

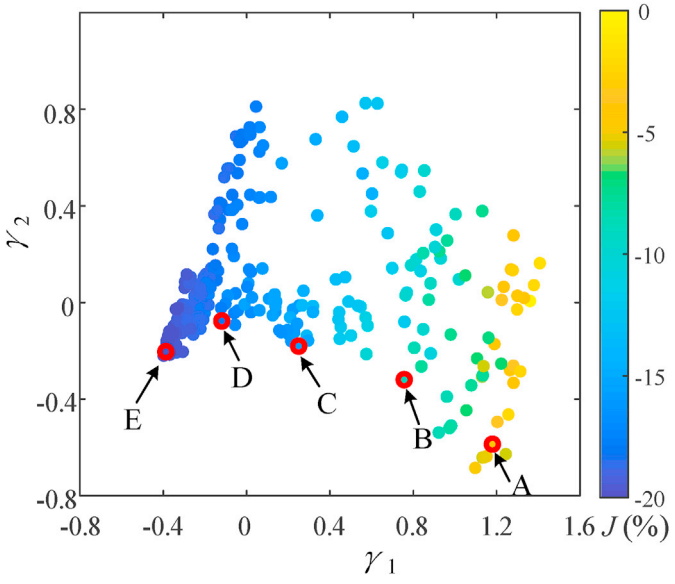

Fig. 8. Proximity map of the control individuals for generations (n = 1, 5, 10, 15, 20 and 25). Each dot represents a control individual and the distance between two control individuals approximates their respective dissimilarity. The black arrows and the red circles indicate five representative cases (A–E), whose details are shown in Table 3. (For interpretation of the references to color in this figure legend, the reader is referred to the Web version of this article.)

1979), which facilitates the understanding of the learning process of genetic algorithm. The MDS could optimally visualize the high-dimensional data in a low-dimensional feature space. For this purpose, the discrepancy between two control individuals is quantified using a distance matrix $C = (C_{l,q})_{1\le l,q\le 25N}$, where $25N$ is the total number of the control individuals in our experiment. Here, $C_{l,q}$ denotes the distance between the individuals b_l and b_q, and is defined by

$$C_{l,q} = \sqrt{|b_l(t) - b_q(t)|^2} + \alpha|J_l - J_q| \tag{8}$$

The first term is the average difference between the l^{th} and q^{th} control individuals, and the second represents a penalization based on the difference of their J. The coefficient α is used to smooth the control landscape in the feature space and is chosen so that the maximum actuation distance of the first term is equal to the maximum performance difference in the second term. The reader is referred to Duriez et al. (2016) for further details. Fig. 8 shows the mentioned proximity map of genetic algorithm process for the generations. For visual clarity, the data are displayed every fifth generation. Each dot represents a control individual, colored with J and the distance between two control individuals approximates their respective dissimilarity. Here, γ_1 and γ_2 are two eigenvectors corresponding to the two largest eigenvalues of C. The first feature coordinate γ_1 clearly correlates with J drawing a parabolic curve, while the second γ_2 plays a less dominant role in improving control performance due to the scattered distribution correlating with J. However, the γ_2 has an important impact on drag reduction in the neighborhood of J = - 20%, where J converges on the rightmost side of the curve presented in Fig. 8. The black arrows and the red circles indicate five representative cases (A – E), whose details are shown in Table 3. Comparing case B to D, one can clearly see the dominant effect of f_1^* on drag reduction when the f_2^*, U_{afc1}^* and U_{afc2}^* have very similar values. The drag reduction is 9% and 18% for cases B and D, respectively, where the change of f_1^* from 4.01 to 1.33 is responsible for a 9% drag reduction. It is reasonable that the $f_1^* = 1.33$ is in the most effective control frequency range, which produces 17% of drag reduction for the S_1 control shown in Fig. 5b. Cases C and D produce 15.3% and 18% drag reduction, respectively, where the f_2^* and U_{afc1}^* show a substantial difference between two cases. This result indicates that the adjustment of f_2^*, together with the increased U_{afc1}^*, contributes to a further 2.7% drag reduction. The f_2^* varies from 5.10 (case C) to 3.87 (case D), which is close to that (3.84) found in the optimal control of case E. All these observations further suggest that the genetic algorithm can gradually optimize the control parameters on the leeward and windward sides, thus improving the control performance.

In order to further understand the optimization process, Fig. 9 displays the probability density function (pdf) P of f_1, f_2, U_{afc1} and U_{afc2} in generations n = 1, 5, 15 and 25. All the distributions of P exhibit an approximate flat shape in the first generation, which arises from the randomly generated f_1, f_2, U_{afc1} and U_{afc2}, as introduced in Sec. 3. As n increases, a significantly pronounced peak gradually appears on P (f_1) and P (U_{afc1}) for $n \ge 5$, while on P (f_2) and P (U_{afc2}) for $n \ge 15$. In other words, the genetic algorithm firstly finds the optimal parameters (f_1, U_{afc1}) on the leeward side and then tunes the control parameters (f_2, U_{afc2}) on the windward side until the optimum control performance is obtained. When the optimal parameters have been found for both the leeward and windward sides, J outperforms that for n = 5, as shown in Fig. 7. Again, the less pronounced peaks in P (f_1), P (U_{afc1}), P (f_2) and P (U_{afc2}) represent that the learning process of genetic algorithm continues to explore other new individuals in all the generations but fails to find better minima of the J, as schematically illustrated in Fig. 6.

Compared to the single frequency control, the input control energy for the optimal control has been reduced slightly, while its drag reduction is improved. The energy efficiency η is defined as follows.

$$I_e = \frac{1}{2}N_a B\rho\left[\left(\frac{2}{T_1}\right)\int_0^{\frac{T_1}{2}} U_{\text{afc1,t}}^3(t)dt + \left(\frac{2}{T_2}\right)\int_0^{\frac{T_2}{2}} U_{\text{afc2,t}}^3(t)dt\right], \tag{9}$$

$$I_0 = \frac{1}{2}\rho W^2 U_\infty^3(-J) \tag{10}$$

$$\eta = \frac{I_0}{I_e} \tag{11}$$

where I_e is the power of the zero-net mass-flux jet and represents an indicator of the energy consumed by the actuators. I_0 is the power saved by the drag reduction. T_1 and $U_{\text{afc1,t}}$ are the actuation period and the real-

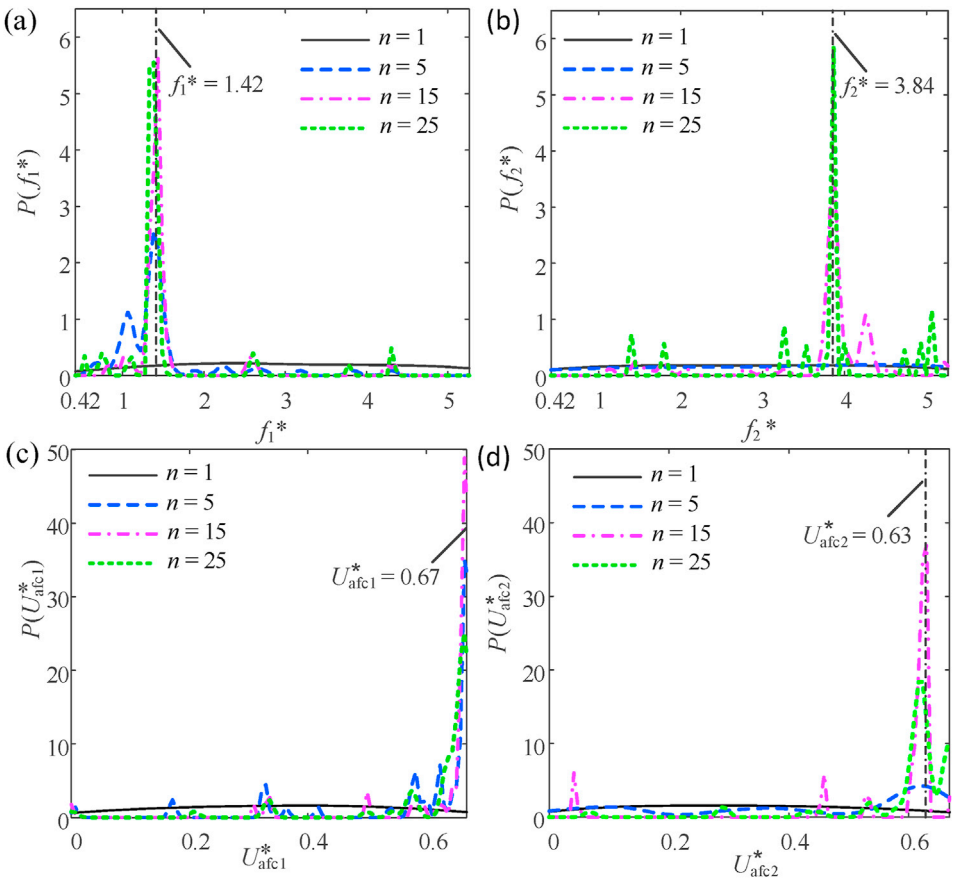

Fig. 9. The probability density function P for f_1, f_2, U_{afc1} and U_{afc2} for the control individuals in the generations (n = 1, 5, 15, and 25). f_1^*, $f_2^* \in$[0.42, 5.3], U_{afc1}^*, $U_{afc2}^* \in$[0, 0.67].

time jet velocity for the S_1 A-pillar. T_2 and $U_{afc2,t}$ are the actuation period and the real-time jet velocity for the S_2 A-pillar. η provides a measure for energy saved from the drag reduction as per unit energy consumed by the actuators. For the single frequency control, I_e and I_0 can be estimated as 1.36 W and 120 W, respectively, given $f^* = 1.54$, $U_{afc}^* = 0.67$ and $J = -17\%$ presented in Fig. 5a. Apparently, this is a highly efficient control system with a η equal to 88. For the optimal control, I_e is 1.25 W and I_0 is 142 W given $f_1^* = 1.42$, $f_2^* = 3.84$, $U_{afc1}^* = 0.67$ and $U_{afc2}^* = 0.63$. Thus, η is 114. As a result, η for the optimal control has been improved by 30% compared to the single frequency control. This result further implies that although the cost function is drag reduction, the genetic algorithm outperforms the single frequency control in terms of energy efficiency due to the increased drag reduction.

5. Flow Physics

Fig. 10 shows the power spectra of the drag force for different observed cases. Here, we find the natural frequencies of the bluff body mechanic system when the set-up is activated with a collision at $U_\infty = 0$ m/s. In contrast to other cases, the power spectra of F_d are shown for the collision case because $\overline{P}_{dyn}$ is zero in Eq. (3). Appreciably, the natural frequencies of the mechanic bluff-body system are found as the predominant component frequencies of $f^* = 0.14$–0.16 with the pronounced peak. It is noticeable that the frequencies for the pronounced peak remain unchanged for no control case at $U_\infty = 19$ m/s, which further confirms that the frequencies of $f^* = 0.14$–0.16 are physically related to the natural frequencies of mechanic system. The peak value at these frequencies can provide a measure for the stability of mechanic system under the actuated control. Compared to no control case, there is an appreciable decrease on the peak at $f^* = 0.14$–0.16 for both the single frequency

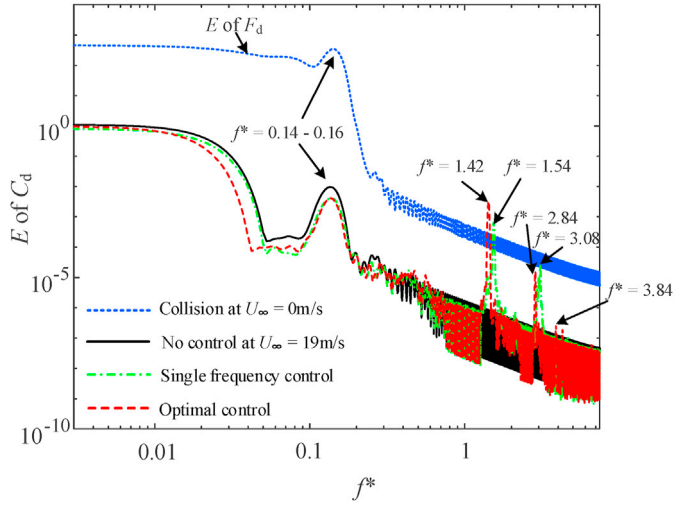

Fig. 10. Power spectra of drag force under different control parameters. Single frequency control: $f^* = 1.54$, $U_{afc}^* = 0.67$; Optimal control: $f_1^* = 1.42$, $f_2^* = 3.84$, $U_{afc1}^* = 0.67$, $U_{afc2}^* = 0.63$.

control ($f^* = 1.54$, $U_{afc}^* = 0.67$; 17% drag reduction shown in Fig. 5a) and the optimal control (20% drag reduction). A negligible difference on the peak value is observed between the two controlled cases with a small difference of 3% drag reduction. These results imply a large suppression on the vibration of bluff body, signifying that the actuations have stabilized the flow around bluff body. In addition, the second super harmonics

$f^* = 3.08$ and 2.84 are also observed for the input control frequencies $f^* = 1.54$ and $f_1^* = 1.42$, respectively, which result from the single frequency control and the optimal control.

Insight may be gained into the control mechanism by examining the flow behaviors in the wake of model. The streamwise velocity U was measured using two calibrated hot wires over $(x/W, y/W) = (0.11–1.50, 0.35–0.65)$ and $(x/W, y/W) = (0–1.39, -0.65$ to $-0.35)$ at $z = 0$. A 2D map of the velocity field and its r.m.s (root mean square) value is therefore created for the unactuated and three controlled cases, as reported in Figs. 11–13. The subscript '*rms*' represents the r.m.s value of the streamwise fluctuation velocity u visualized in Figs. 12 and 13.

Comparing the case without control to the S_2 control, the flow separation has been largely suppressed on the windward side while enlarged on the leeward side, as reported in Fig. 11 (a, b) and 12 (a, b). For the windward side, the core area of flow separation is found at $y/W = -0.58$ for the line $x/W = 0$, where the maximum u_{rms}^* takes place. The representative area is chosen as $(x/W, y/W) = (0–0.21, -0.65 – -0.60)$ in the upper leftmost corner of the measured area, i.e., the outer flank of flow separation indicated by a red dotted rectangle in Fig. 11 (a, b) and 12 (a, b). The averaged $\overline{U}^*$ is 0.907 in this area for no control case, 6% less than that (0.963) for the S_2 control. Meanwhile, the averaged u_{rms}^* substantially reduces from 0.197 to 0.158 for the latter case. Correspondingly, the level of $\overline{U}^* = 1.0$ shrinks from $y/W = -0.65$ to -0.625 at $x/W = 0$ (Fig. 13a) and the u_{rms}^* substantially drops from 0.18 to 0.13 at $(x/W, y/W) = (0, -0.65)$ (Fig. 13d). These results imply that the S_2 control reduces the flow separation and stabilizes the flow on the windward side. For the leeward side, the blue lines represent the core of flow separation and the measured area is in the inner flank of flow separation. The maximum values for both $\overline{U}^*$ and u_{rms}^* are found in the bottom rightmost corner of the measured area presented in Fig. 11 (a, b) and 12 (a, b). The area of $\overline{U}^* \geq 0.4$ and $u_{rms}^* \geq 0.2$ is 3.8 and 2.2 times larger for no control than the S_2 control, respectively. Furthermore, there is a decrease on both $\overline{U}^*$ (Fig. 13b) and u_{rms}^* (Fig. 13e) over the range of $y/W = 0.35–0.65$ at $x/W = 0.11$ for the latter case. Both $\overline{U}^*$ (Fig. 13c) and u_{rms}^* (Fig. 13f) have a slight reduction over the range of $x/W = 0.11–1.50$ at $y/W = 0.65$. These observations suggest that the core of flow separation moves away from the bluff body and the flow separation is enlarged on the leeward side for the S_2 control. Li et al. (2017) performed experiments using the pulsed jet control at all trailing edges of a blunt-edged Ahmed body and obtained 22% drag reduction. They indicated that the recirculation bubble became shorter and narrower in the controlled wake, resulting in an increase of the base pressure recovery and a consequent reduction of drag. Therefore, it may be inferred that the reduction of flow separation would lead to a drag reduction while the enlargement of separation bubble would have a negative impact on drag. As a result, the S_2 control produces a drag reduction of 1.5% due to the balance between a reduction of flow separation at the windward side and an enlargement at the leeward side.

The drag reduction is 17% and 20% for the S_1 control and the optimal control, respectively, which also results from the balance of flow separation on the windward and leeward sides. Comparing the case without control to the S_1 control, the $\overline{U}^*$ decreases from 1.0 to 0.91 (Fig. 13a) while the u_{rms}^* increases from 0.18 to 0.20 at the upper leftmost point $(x/W, y/W) = (0, -0.65)$ for the measured area at windward side (Fig. 13d). For the leeward side, the high contours of $\overline{U}^* = 0.3–0.6$ and $u_{rms}^* = 0.21–0.22$ emerge and cover the significant part of the measured area for the S_1 control, as represented in Figs. 11c and 12c. The S_1 control brings a substantial increase of $\overline{U}^*$ between $y/W = 0.58–0.65$ (Fig. 13b) and u_{rms}^* between $y/W = 0.45–0.65$ at $x/W = 0.11$ (Fig. 13e). Meanwhile, a significant increase is observed on $\overline{U}^*$ over $x/W = 0.11–1.50$ (Fig. 13c) and u_{rms}^* over $x/W = 0.11–1.20$ at $y/W = 0.65$ (Fig. 13f). These results unequivocally indicate that the S_1 control produces a drag reduction of 17%, where a reduction of flow separation is observed on the leeward side and an enlargement on the windward side. When the S_2 control is combined with the S_1 control, the optimal control exploits the reduction effect of flow separation for both the leeward and windward sides. The optimal control has a very similar distribution of $\overline{U}^*$ (Fig. 11b, d and 13a) and u_{rms}^* (Fig. 12b, d and 13d) compared to the S_2 control for flow field on the windward side, where the flow separation is largely suppressed. For the leeward side, similar behaviors are observed for $\overline{U}^*$ (Fig. 11c, d, 13b and 13c) and u_{rms}^* (Fig. 12c, d, 13e and 13f) for the S_1 control and the optimal control. This means there is a substantial reduction of flow separation on the leeward side for the latter control case. Thus, the optimal control obtains the highest drag reduction of 20%. As a consequence, these observations reveal that genetic algorithm can obtain the optimized control parameters, which reduce the separation region on the leeward and windward sides in the wake, further stabilizing the bluff body system and improving the control performance.

It is noteworthy to observe that the flow separation is enlarged to obtain a drag reduction of 20% for the bluff body with 0-degree yaw angle in Minelli et al. (2020), where the wake extends by 40% compared to the uncontrolled case. The observation is apparently different from the present study with the suppressed separation under the optimal control, which may be ascribed to the Reynolds number and the yaw angle of 10°. The present Reynolds number is 12 times that of Minelli et al. (2020), where the high Reynolds number would reduce the flow separation at the front edges and the drag coefficient (Cooper 1985), as described in Sec. 2.1. Once yaw angle is introduced, most of the free-stream flow enters wake region on the leeward side and a large recirculating motion occurs to form a large low-pressure zone close to the leeward edge (Li et al., 2019). Meanwhile, the drag coefficient grows as the yaw angle increases from zero to 60° (Bello-Millan et al., 2016). Therefore, it is reasonable for the present study to significantly reduce the separation on the leeward side, which greatly contributes to drag reduction.

The power spectra E of u are examined in Fig. 14 to illustrate the important relationship between the suppressed wake structures and the observed drag reduction. On the windward side, two representative locations of H and I are chosen in the upper and bottom corner of the measured area, i.e., $y/W = -0.65$ and -0.35 at $x/W = 0$. They are located at the outer and the inner layers of the flow separation region as described in Figs. 11–13. Comparing to no control case, there is an appreciable decrease in E under the optimal control for both H and I locations, especially over relatively low frequencies $f^* < 0.30$. In other words, this observation indicates that the actuations greatly reduce the energy of turbulent structures in the wake, especially for the large-scale structures on the windward side. This result is fully consistent with the measurement of Grandemange et al. (2015), where the optimally chamfered angles at the trailing edges result in the absence of large-scale vortices in the wake of an Ahmed body geometry, obtaining 5.8% of drag reduction. In addition, for the optimal control, two pronounced peaks appear at $f^* = 1.42$ and 3.84 in Fig. 14a at the outer layer of the flow separation region, which results from the input control frequencies in Fig. 10.

For the leeward side, there is a significant suppression on the dynamics of wake structures at the inner layer of the flow separation under the optimal control, which further contributes to a substantial reduction of flow separation and reducing drag. Similar to the windward side, the other two locations are set as J and K on the leeward side, i.e., $y/W = 0.35$ and 0.65 at $x/W = 0.11$ in Figs. 11–13. As shown in Fig. 14c, a significant decrease takes place in E over the entire frequencies f^* for J under the optimal control, which locates at the inner layer of the flow separation region. Meanwhile, an increase is observed in E for K at the outer layer (Fig. 14d). These results signify that the actuations suppress the wake dynamics in the inner layer of the flow separation region and force the streamwise high-speed fluid to move closer to the bluff body, thus reducing the flow separation on the leeward side. This is consistent with the observation in Figs. 11–13.

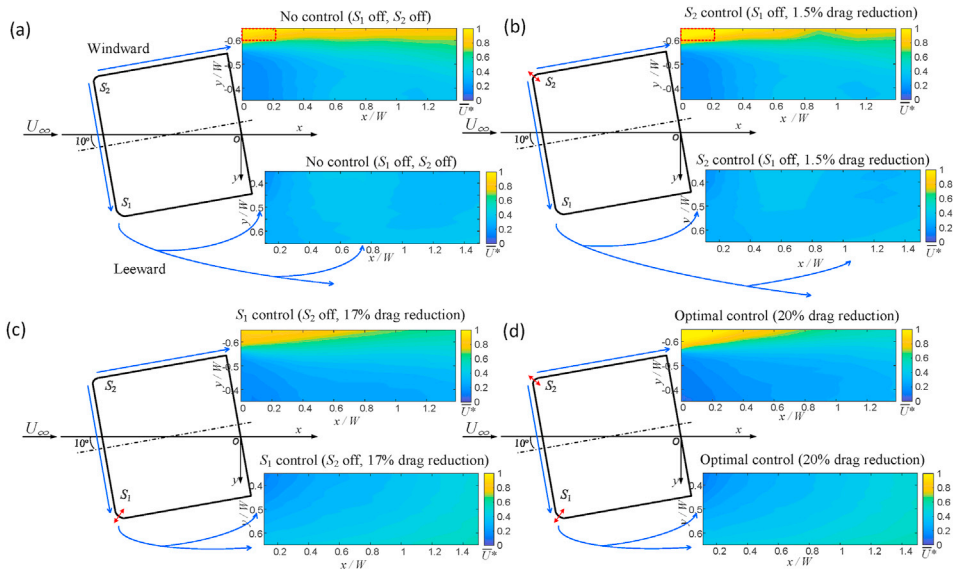

Fig. 11. Iso-contours of $\overline{U}$ in the wake of bluff body. (a) No control: The actuators are unactuated (S_1: off, S_2: off); (b) S_2 control. S_2: $f_2^* = 3.84$, $U_{afc2}^* = 0.63$, S_1: off; (c) S_1 control. S_2: off, $S1$: $f_1^* = 1.42$, $U_{afc1}^* = 0.67$; (d) Optimal control. S_1: $f_1^* = 1.42$, $U_{afc1}^* = 0.67$, S_2: $f_2^* = 3.84$, $U_{afc2}^* = 0.63$.The contour resolution is $\Delta = 0.04$. The red arrows indicate the actuation position and the blue lines represent an interpretation of the flow separation around bluff body. $U_\infty = 19$ m/s. (For interpretation of the references to color in this figure legend, the reader is referred to the Web version of this article.)

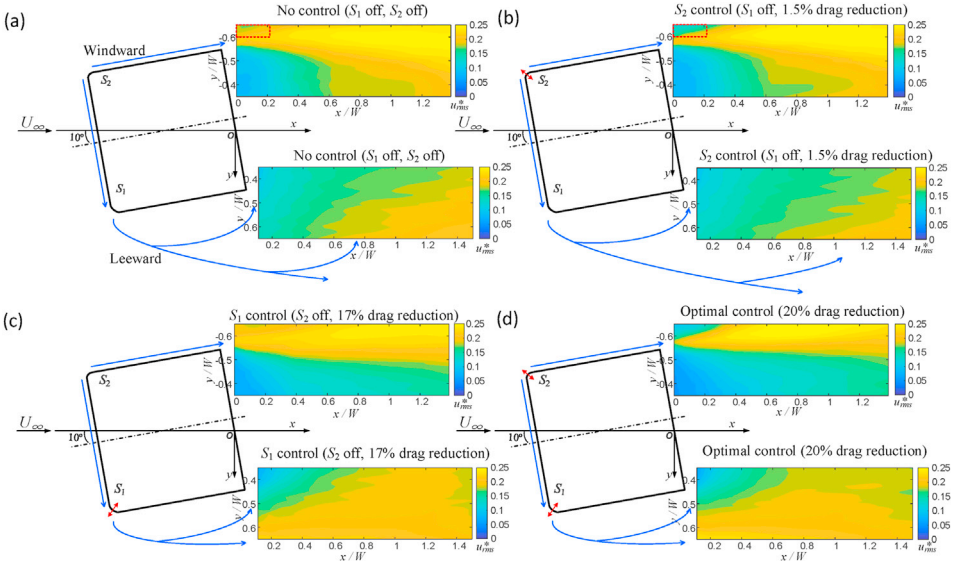

Fig. 12. Iso-contours of u_{rms} in the wake of bluff body. Refer to Fig. 11 for the control parameters in (a), (b), (c) and (d).The contour resolution is $\Delta = 0.01$. The red arrows indicate the actuation position and the blue lines represent the flow separation around bluff body. $U_\infty = 19$ m/s. (For interpretation of the references to color in this figure legend, the reader is referred to the Web version of this article.)

6. Conclusions

This work experimentally aims to manipulate the bluff body at a yaw angle of 10° for the purpose of reducing drag. Two loudspeakers are used to generate zero-net mass-flux jet through streamwise slots, which span a large portion of the rounded A-pillars of bluff body. Compared to traditionally vertical slot actuation (Minelli et al., 2017), the streamwise slot actuation is not affected by the separation point and not only works effectively for bluff bodies with a yaw angle of zero (e.g. Minelli et al., 2019) but also for yaw angles. The actuations produce a maximum drag reduction of 17% and 2% for the leeward and windward side control, respectively. When the actuations on both the leeward and windward sides are activated using the same sinusoidal signal, the single frequency control obtains a maximum drag reduction of 17%. Furthermore, this upstream control strategy is a highly efficient control system with an energy efficiency η of 79 for the single frequency control.

A genetic algorithm is used to optimize a multi-frequency control, where two sinusoidal signals are used to separately control the actuators on the leeward and windward sides. Thus, four parameters have been investigated, i.e., two frequencies (f_1, f_2) and two peak jet velocities (U_{afc1}, U_{afc2}). The optimal control parameters from genetic algorithm have been found as $f_1^* = 1.42$, $f_2^* = 3.84$, $U_{afc1}^* = 0.67$ and $U_{afc2}^* = 0.63$. The maximum drag reduction achieved is 20%, 3% larger than 17% attained from the single frequency control. As a consequence, the optimal control improves the energy efficiency by 30%.

The measured data from the force balance and hot wires are analyzed to find out the flow mechanism behind the control. The power spectra of the drag indicate that the energy at the natural frequencies of $f^* = 0.14$–0.16 has been reduced under the control, resulting in a large suppression on the vibration of the bluff body. Under the optimal control, the vortex shedding has been reduced substantially on both the windward and leeward sides in the wake. The power spectra of the streamwise

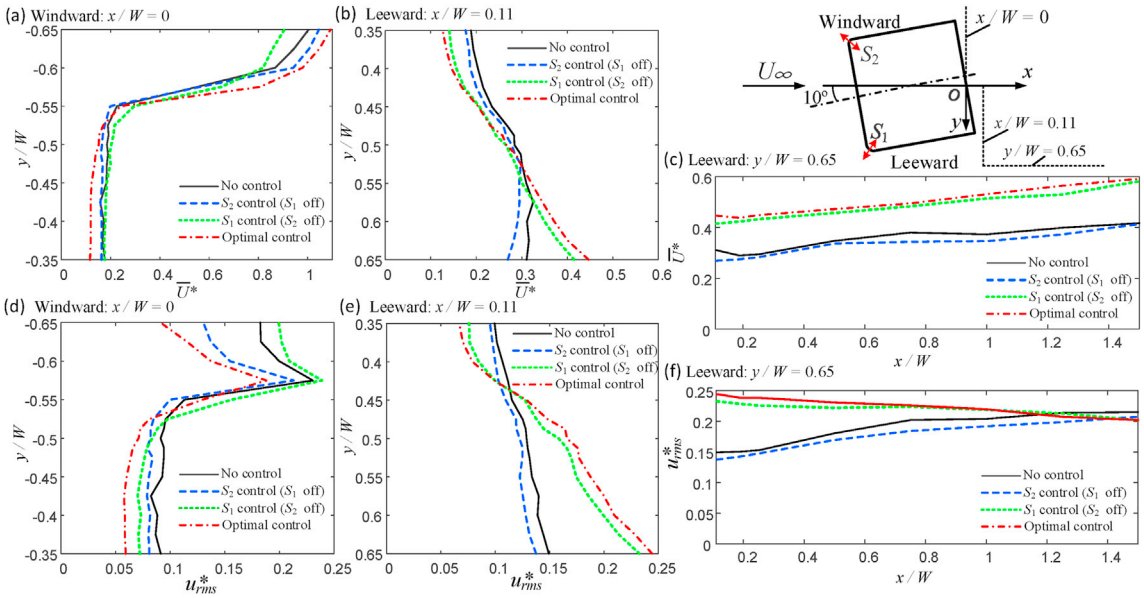

Fig. 13. Distributions of (a) $\overline{U} - y$ at $x/W = 0$, (b) $\overline{U} - y$ at $x/W = 0.11$, (c) $\overline{U} - x$ at $y/W = 0.65$, (d)$u_{\mathrm{rms}} - y$ at $x/W = 0$, (e)$u_{\mathrm{rms}} - y$ at $x/W = 0.11$, (f)$u_{\mathrm{rms}} - x$ at $y/W = 0.65$. The control parameters are as in Fig. 11. $U_\infty = 19$ m/s.

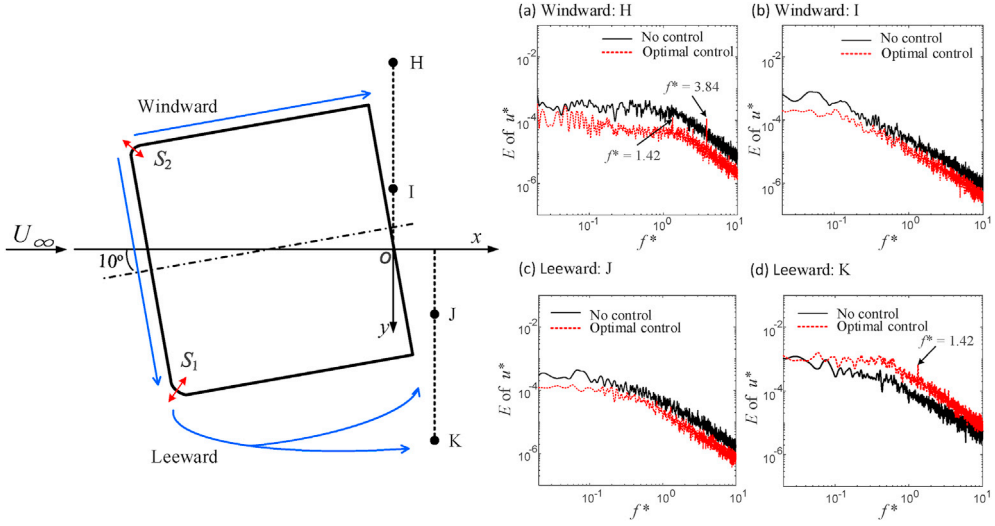

Fig. 14. Power spectra E of u at different locations of (a) H: $(x/W, y/W) = (0, -0.65)$, (b) I: $(x/W, y/W) = (0, -0.35)$, (c) J: $(x/W, y/W) = (0.11, 0.35)$ and (d) K: $(x/W, y/W) = (0.11, 0.65)$ under different control parameters. The control parameters are as in Fig. 11. $U_\infty = 19$ m/s.

fluctuation velocity illustrate the important relationship between the suppressed wake structures and the observed drag reduction. All the observations highlight that the perturbation produced by the actuators suppresses the wake dynamics, stabilizes the bluff body system, and reduces the flow separation region, which are fully consistent with the drag reduction.

Working on optimizing the interaction between the actuation and the near-wall turbulent structures on the leeward and windward sides, the present genetic algorithm tunes the control parameters based on a trial-and-error method until the optimum control performance is obtained. This genetic algorithm technique provides a useful tool that outperforms the single-frequency control strategy in terms of the maximum drag reduction. For future works, a genetic algorithm optimization strategy, combining upstream and downstream direct-wake control, is expected to develop to further improve control performance for bluff bodies with or without yaw angle.

CRediT authorship contribution statement

Z.X. Qiao: Methodology, Investigation, Software, Writing – original draft, preparation. **G. Minelli:** Data curation, Validation, Writing-reviewing and editing. **B.R. Noack:** Conceptualization, Methodology, Resources, Supervision. **S. Krajnović:** Conceptualization, Methodology, Resources, Funding acquisition, Supervision. **V. Chernoray:** Software, Conceptualization, Methodology, Supervision.

Declaration of competing interest

The authors declare that they have no conflict of interest.

Acknowledgements

Current work was funded and supported by Chalmers University of

Technology on experimental facilities provided by Chalmers Laboratory of Fluids and Thermal Sciences. QZX wishes to thank the support from NSFC through grant No. 12002098.

References

Abbassi, M.R., Baars, W.J., Hutchins, N., Marusic, I., 2017. Skin-friction drag reduction in a high-Reynolds-number turbulent boundary layer via real-time control of large-scale structures. Int. J. Heat Fluid Flow 67, 30–41.

Aubrun, S., McNally, J., Alvi, F., Kourta, A., 2011. Separation flow control on a generic ground vehicle using steady microjet arrays. Exp. Fluid 51 (5), 1177–1187.

Beaudoin, J.F., Aider, J.L., 2008. Drag and lift reduction of a 3D bluff body using flaps. Exp. Fluid 44, 491–501.

Bello-Millan, F.J., Mäkelä, T., Parras, L., Del Pino, C., Ferrera, C., 2016. Experimental study on Ahmed's body drag coefficient for different yaw angles. J. Wind Eng. Ind. Aerod. 157, 140–144.

Bonnavion, G., Cadot, O., 2019. Boat-tail effects on the global wake dynamics of a flat-backed body with rectangular section. J. Fluid Struct. 89, 61–71.

Brunton, S.L., Noack, B.R., 2015. Closed-loop turbulence control: progress and challenges. Appl. Mech. Rev. 67 (5), 050801.

Brunton, S.L., Noack, B.R., Koumoutaskos, P., 2020. Machine learning for fluid mechanics. Annu. Rev. Fluid Mech. 52, 477–508.

Choi, H., Moin, P., Kim, J., 1994. Active turbulence control for drag reduction in wall-bounded flows. J. Fluid Mech. 262, 75–110.

Cooper, K.R., 1985. The effect of front-edge rounding and rear-edge shaping on the aerodynamic drag of bluff vehicles in ground proximity. SAE Pap. 850288. SAE Int., Warrendale, PA.

Duriez, T., Brunton, S.L., Noack, B.R., 2016. Machine. In: Learning Control — Taming Nonlinear Dynamics and Turbulence. Series "Fluid Mechanics and its Applications", No. 116. Springer, Berlin.

Grandemange, M., Cadot, O., Courbois, A., Herbert, V., Ricot, D., Ruiz, T., Vigneron, R., 2015. A study of wake effects on the drag of Ahmed's squareback model at the industrial scale. J. Wind Eng. Ind. Aerod. 145, 282–291.

Grandemange, M., Gohlke, M., Cadot, O., 2013. Turbulent wake past a three-dimensional blunt body. Part 1. Global modes and bi-stability. J. Fluid Mech. 722, 51–84.

Hammond, E.P., Bewley, T.R., Moin, P., 1998. Observed mechanisms for turbulence attenuation and enhancement in opposition-controlled wall bounded flows. Phys. Fluids 10 (9), 2421–2423.

Howell, J., Passmore, M., Windsor, S., 2018. A drag coefficient for test cycle application. SAE International Journal of Passenger Cars-Mechanical Systems 11, 447–461.

Kasagi, N., Suzuki, Y., Fukagata, K., 2009. Microelectromechanical systems–based feedback control of turbulence for skin friction reduction. Annu. Rev. Fluid Mech. 41, 231–251.

Kim, J., Bewley, T., 2007. A linear systems approach to flow control. Annu. Rev. Fluid Mech. 39, 383–417.

Koumoutsakos, P., Freund, J., Parekh, D., 2001. Evolution strategies for automatic optimization of jet mixing. AIAA J. 39 (5), 967–969.

Krajnović, S., Davidson, L., 2003. Numerical study of the flow around a bus-shaped body. J. Fluid Eng. 125 (3), 500–509.

Li, R., Noack, B.R., Cordier, L., Borée, J., Harambat, F., 2017. Drag reduction of a car model by linear genetic programming control. Exp. Fluid 58 (8), 103.

Li, R., Borée, J., Noack, B.R., Cordier, L., Harambat, F., 2019. Drag reduction mechanisms of a car model at moderate yaw by bi-frequency forcing. Physical Review Fluids 4 (3), 034604.

Ligrani, P.M., Bradshaw, P., 1987. Spatial resolution and measurement of turbulence in the viscous sublayer. Exp. Fluid 5 (6), 407–417.

Mardia, K.V., Kent, T.J., Bibby, J.M., 1979. Multivariate Analysis. Probability and Mathematical Statistics. Academic Press.

Minelli, G., Krajnović, S., Basara, B., Noack, B.R., 2016. Numerical investigation of active flow control around a generic truck A-pillar. Flow, Turbul. Combust. 97 (4), 1235–1254.

Minelli, G., Hartono, E.A., Chernoray, V., Hjelm, L., Krajnović, S., 2017. Aerodynamic flow control for a generic truck cabin using synthetic jets. J. Wind Eng. Ind. Aerod. 168, 81–90.

Minelli, G., Tokarev, M., Zhang, J., Liu, T., Chernoray, V., Basara, B., Krajnović, S., 2019. Active aerodynamic control of a separated flow using streamwise synthetic jets. Flow, Turbul. Combust. 103 (4), 1039–1055.

Minelli, G., Krajnović, S., Basara, B., 2018. A flow control study of a simplified, oscillating truck cabin using PANS. J. Fluid Eng. 140 (12), 121101.

Minelli, G., Dong, T., Noack, B.R., Krajnović, S., 2020. Upstream actuation for bluff-body wake control driven by a genetically inspired optimization. J. Fluid Mech. 893, 1–28.

Pirau, S., Raghav, V., Forbes, A., Liberi, B., Komerath, N., 2014. Efficient airload determination for bluff body aeromechanics. In: ASME 2014 International Mechanical Engineering Congress and Exposition. American Society of Mechanical Engineers Digital Collection.

Pujals, G., Depardon, S., Cossu, C., 2010. Drag reduction of a 3D bluff body using coherent streamwise streaks. Exp. Fluid 49 (5), 1085–1094.

Qiao, Z.X., Wu, Z., Zhou, Y., 2018. Turbulent boundary layer manipulation under a proportional-derivative closed-loop scheme. Phys. Fluids 30 (11), 115101.

Qiao, Z.X., Zhou, Y., Wu, Z., 2017. Turbulent boundary layer under the control of different schemes. Proc. R. Soc. A 473, 20170038.

Rabault, J., Kuchta, M., Jensen, A., Réglade, U., Cerardi, N., 2019. Artificial neural networks trained through deep reinforcement learning discover control strategies for active flow control. J. Fluid Mech. 865, 281–302.

Rapoport, D., Fono, I., Cohen, K., Seifert, A., 2003. Closed-loop vectoring control of a turbulent jet using periodic excitation. J. Propul. Power 19 (4), 646–654.

Rathnasingham, R., Breuer, K.S., 2003. Active control of turbulent boundary layers. J. Fluid Mech. 495, 209–233.

Ren, F., Hu, H., Tang, H., 2020. Active flow control using machine learning: a brief review. J. Hydrodyn. 32 (2), 247–253.

Rowley, C.W., Dawson, S.T., 2017. Model reduction for flow analysis and control. Annu. Rev. Fluid Mech. 49, 387–417.

Schmidt, H.J., Woszidlo, R., Nayeri, C.N., Paschereit, C.O., 2015. Drag reduction on a rectangular bluff body with base flaps and fluidic oscillators. Exp. Fluid 56 (7), 1–16.

Seifert, A., Greenblatt, D., Wygnanski, I.J., 2004. Active separation control: an overview of Reynolds and Mach numbers effects. Aero. Sci. Technol. 8 (7), 569–582.

Seifert, A., Stalnov, O., Sperber, D., Arwatz, G., Palei, V., David, S., Dayan, I., Fono, I., 2009. Large trucks drag reduction using active flow control. In: The Aerodynamics of Heavy Vehicles II: Trucks, Buses, and Trains. Springer, Berlin, Heidelberg, pp. 115–133.

Tokarev, M., Minelli, G., Zhang, J., Noack, B.R., Chernoray, V., Krajnović, S., 2019. PIV Measurements Around a Generic Truck Model in Active Flow Control Experiments. 13th International Symposium on Particle Image Velocimetry – ISPIV (Munich, Germany).

Wahde, M., 2008. Biologically Inspired Optimization Methods: an Introduction. WIT press.

Zhou, Y., Fan, D., Zhang, B., Li, R., Noack, B.R., 2020. Artificial intelligence control of a turbulent jet. J. Fluid Mech. 897, 1–46.

Zhang, B.F., Liu, K., Zhou, Y., To, S., Tu, J.Y., 2018. Active drag reduction of a high-drag Ahmed body based on steady blowing. J. Fluid Mech. 856, 351–396.

Zhang, M.M., Cheng, L., Zhou, Y., 2004. Closed-loop-controlled vortex shedding and vibration of a flexibly supported square cylinder under different schemes. Phys. Fluids 16 (5), 1439–1448.